Mapping the Conductance of Electronically Decoupled Graphene Nanoribbons

Peter H. Jacobse, Mark J. J. Mangnus, Stephan J. M. Zevenhuizen, and Ingmar Swart*

Debye Institute for Nanomaterials Science, Utrecht University, P.O. Box 80000, 3508 TA Utrecht, The Netherlands

S Supporting Information

ABSTRACT: With the advent of atomically precise synthesis and consequent precise tailoring of their electronic properties, graphene nanoribbons (GNRs) have emerged as promising building blocks for nanoelectronics. Before being applied as such, it is imperative that their charge transport properties are investigated. Recently, formation of a molecular junction through the controlled attachment of nanoribbons to the probe of a scanning tunneling microscope (STM) and subsequent lifting allowed for the first conductance measurements. Drawbacks are the perturbation of the intrinsic electronic properties through interaction with the metal surface, as well as the risk of current-induced defect formation which largely restricts the measurements to low bias voltages. Here, we show that resonant transport—essential for device applications—can be measured by lifting electronically decoupled GNRs from an ultrathin layer of NaCl. By varying the applied voltage and tip−sample distance, we can probe resonant transport through frontier orbitals and its dependence on junction length. This technique is used for two distinct types of GNRs: the 7 atom wide armchair GNR and the 3,1-chiral GNR. The features in the conductance maps can be understood and modeled in terms of the intrinsic electronic properties of the ribbons as well as capacitive coupling to tip and substrate. We demonstrate that we can simultaneously measure the current decay with increasing junction length and bias voltage by using a double modulation spectroscopy technique. The strategy described in this work is widely applicable and will lead to a better understanding of electronic transport through molecular junctions in general.
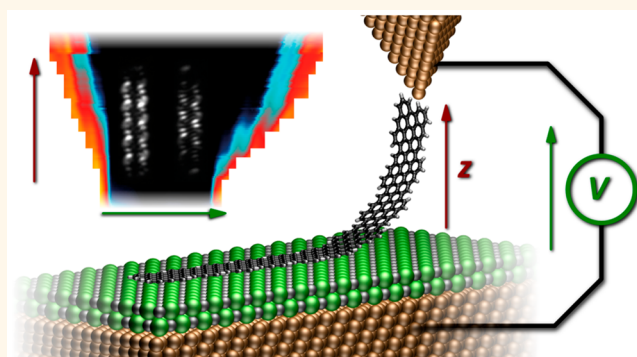
KEYWORDS: graphene nanoribbons, scanning tunneling microscopy, molecular conductance, electronic structure, charge transport

The discovery of graphene's exceptional electronic properties[1−3] has initiated a quest for a new generation of graphene-based electronic devices. The absence of a band gap, however, has impeded the application of the two-dimensional material in electronics. A band gap can be introduced into graphene through quantum confinement in one of its lateral dimensions, forming graphene nanoribbons (GNRs).[4−7] Because the electronic properties of graphene nanoribbons are sensitively dependent on their width and edge structure, it is important to control fabrication down to the atomic level, a degree of precision that currently cannot be obtained through top-down methods.[8,9] Recently established bottom-up techniques based on on-surface synthesis[10,11] have facilitated the fabrication of atomically well-defined graphene nanoribbons of various widths and edge structures. Notably, numerous types of armchair edge nanoribbons[12−20] (acGNR) have been produced, as well as ribbons with zigzag[21,22] or chiral[23−27] edges, which host low-energy edge-localized states.[3,4,7,28−32] The high degree of control obtained so far has facilitated fabrication of not only atomically precise GNRs of a single type but also heterojunctions, such as metal−

semiconductor junctions,[33] type-I (straddling gap) junctions,[34−37] and type-II (staggered gap) junctions.[38,39] These developments signify a trend of incorporating more functionality into graphene nanoribbons and indicate a maturing of the field toward electronics applications.[36,40]

For applications in molecular electronic devices, it is essential to understand current transport through individual GNRs and how it is impacted by their geometry. Field-effect transistor behavior has been investigated in graphene nanoribbons,[41,42] but for a proper understanding of transport through individual GNRs, nonensemble techniques are required. In a pioneering study by Koch et al., single 7-acGNRs were lifted off a metal substrate with an STM tip, and the voltage-dependent conductance was measured in this lifting geometry.[43] This STM-based conductance measurement methodology was developed earlier for conjugated polymers[44] and has later been used to demonstrate high conductance and
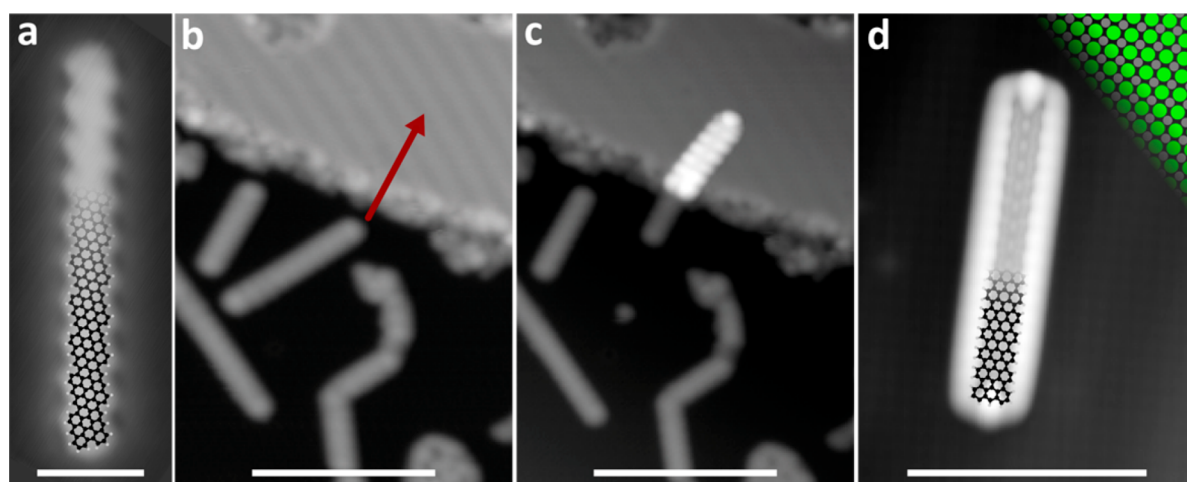
Figure 1. Transfer of graphene nanoribbons onto sodium chloride. (a) STM scan ($V = -1.8$ V, $I = 20$ pA) of a 10 monomer long 3,1-cGNR on Cu(111). The overlay shows a model of the atomic geometry. Scale bar: 2 nm. (b) STM scan ($V = -1.8$ V, $I = 20$ pA) of a 3,1-cGNR before being transferred onto a patch of sodium chloride. Scale bar: 10 nm. (c) STM scan ($V = -1.8$ V, $I = 20$ pA) showing the same nanoribbon after partial transfer onto the sodium chloride. Scale bar: 10 nm. (d) STM scan ($V = -1.8$ V, $I = 20$ pA) of a 7-acGNR on NaCl. A model of the atomic geometry is overlaid, as well as a model of the underlying sodium chloride. Scale bar: 5 nm.

resonant charge transport in different molecular wires.[45,46] This technique has subsequently been used to measure the conductance through metal−semiconductor junctions in GNRs, composed of 5-acGNR and 7-acGNR segments.[33] When a low bias voltage is applied to the tip−GNR−substrate junction, off-resonant transport can be measured, which is characterized by an exponentially decaying current with increasing path length.[33,43] However, at length scales of device geometries, resonant transport is the dominant mechanism. Unfortunately, the risk of current-induced defect formation in STM-based conductance experiments makes it difficult to apply voltages beyond the band gap and access resonant transport without destruction of the junction, particularly at lower tip heights. Furthermore, the intrinsic features of GNRs involved in electronic transport are obscured as molecular states hybridize with metallic states of the substrate.[47,48] In addition, nanoribbons in contact with a metallic substrate may accumulate a (partial) charge or be subject to correlation effects.[47−49] Therefore, although lifting experiments provide a way to access the conductance of single nanoribbons, the influence of the metal substrate can be detrimental for a detailed analysis of the intrinsic resonant transport properties.

It has been demonstrated that molecules can be electronically decoupled from a metal substrate by introducing an intercalating layer of an insulating material such as NaCl.[49,50] Similarly, electronic decoupling of GNRs has been achieved by transfer onto a NaCl monolayer.[21,36,47] Unlike smaller molecules, GNRs cannot directly be deposited onto intercalating layers by means of evaporation. Instead, transfer should be performed *in situ*, using the tip of an STM. This technique relies on the methodology of Koch *et al.*[43] to lift the nanoribbons from the metal substrate, followed by lateral manipulation[51] and deposition (by means of a voltage pulse).[47] Probe-controlled transfer has initially been used on 7-acGNRs on Au(111) but has since then also been applied to zigzag-type nanoribbons[21] and metal−semiconductor heterojunctions composed of laterally fused 7-acGNRs.[36] Large molecular wires have been transferred to NaCl by using a higher coverage of the intercalant. This may be a complementary method to transfer GNRs onto thin insulating films.[50,52]

Our aim in this work is to perform a detailed investigation of the electronic transport through different types of graphene nanoribbons, using the decoupling effect induced by NaCl intercalation to research the inherent, unperturbed conductance properties. Besides electronically decoupling the GNRs from the metal substrate, the introduction of a NaCl layer provides an additional tunnel barrier which dampens the current through the molecular junction. This allows us to probe resonant transport at low tip heights, while simultaneously reducing the risk of destruction of the junction through inelastic processes that were found to become more pronounced at high currents.[43]

We have selected two distinct types of nanoribbons, namely, 7-acGNRs and 3,1-cGNRs, the latter of which have recently emerged as the surprising product of nanoribbon synthesis from bianthryl-type molecules on Cu(111).[23,25,26] Pure 7-acGNRs have experimentally been characterized as wide-band-gap semiconductors.[47,48,53,54] cGNRs, on the other hand, are expected to host a band of topological edge states close to the Fermi level due to the partial zigzag structure of their edges.[29,55,56] Even though a detailed investigation on Au(111) has not revealed a pronounced edge-localized character of the low-bias states, it has been shown that for 3,1-cGNR these states reside at an energy significantly lower than that of the frontier states of 7-acGNR.[57]

Although a detailed investigation of the electronic structure of 7-acGNR on NaCl has been performed,[47] decoupling of 3,1-cGNRs has not yet been reported. Therefore, we first characterize the nature of the frontier states of 3,1-cGNR after transfer onto NaCl by means of scanning tunneling spectroscopy (STS) and differential conductance mapping.[50] Next, we focus on the transport properties of GNRs as a function of tip height (length of the junction) and bias voltage, providing conductance maps in two-dimensional (V,z) space.

Finally, we study the length-dependent current decay as a function of voltage by means of double modulation spectroscopy, where the tip height is modulated using a lock-in amplifier in addition to the one used to monitor the conductance. Specifically, the exponential current decay parameter β was recorded as a function of voltage. This
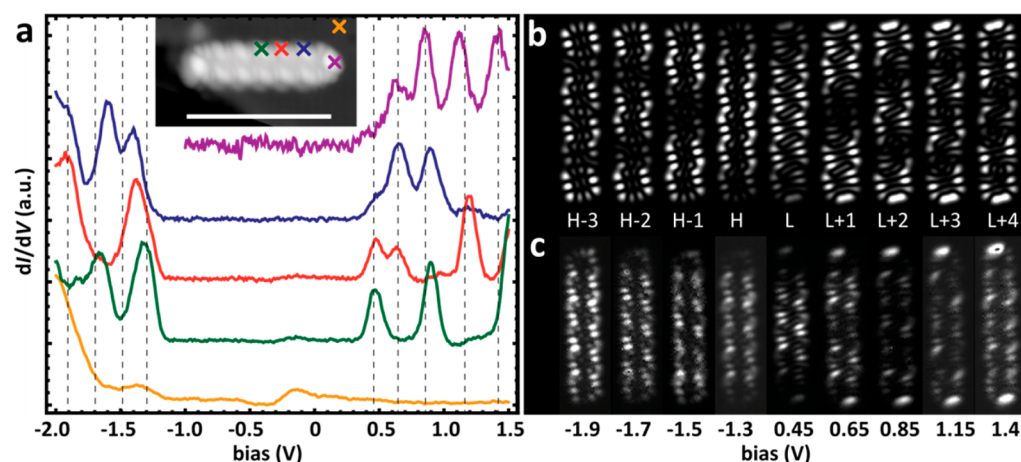
Figure 2. Differential conductance spectroscopy on a decoupled 3,1-cGNR. (a) dI/dV spectra acquired on a 6 monomer long 3,1-cGNR on NaCl. The inset shows an STM scan ($V = -1.8$ V, $I = 20$ pA) of the nanoribbon. The crosses indicate the positions where the spectra were acquired. Scale bar: 5 nm. (b) Simulated differential conductance maps corresponding to the frontier orbitals of the 3,1-cGNR. "H" indicates the highest occupied molecular orbital (HOMO); "L" indicates the lowest unoccupied molecular orbital (LUMO). (c) Differential conductance maps recorded on the 3,1-cGNR, with the respective bias voltages indicated underneath. The bias voltages correspond to the successive peaks in the spectra over the ribbon and should therefore be correlated to the successive states in b.

parameter characterizes the nature of the charge transport: (quasi-)ballistic transport (zero or small β) or nonresonant (large β).[46] The double modulation spectroscopy technique described in this work is applicable to graphene nanoribbons but can equally well be applied to other types of molecular junctions.

RESULTS

Characterization of 3,1-cGNR on NaCl. 3,1-cGNRs were grown on Cu(111) using 10,10′-dichloro-9,9′-bianthryl (DCBA) as described before.[26] After ribbon growth, a submonolayer of NaCl was deposited onto the same substrate, and the sample was transferred into a low-temperature STM housed in the same vacuum system. We transferred 3,1-cGNRs onto NaCl as described using the method described by Wang *et al.*[47] STM scans of a chiral nanoribbon on Cu(111), both before and after being partially dragged onto a NaCl patch, are shown in Figure 1a−c. For comparison, Figure 1d shows an STM scan of a 7-acGNR that has been transferred onto NaCl. Similar to what has been reported for 7-acGNRs, the electronic decoupling of 3,1-cGNRs from the surface due to intercalation immediately presents itself as a large increase in the apparent height and in the appearance of nodal planes.[50] This is true as long as the bias voltage is sufficiently high for resonant tunneling into states of the nanoribbon; the ribbons were found to be highly mobile while scanning in-gap, underlining the weak interaction between the GNR and NaCl.

Figure 2a shows dI/dV spectra recorded on different positions of a 6 monomer long 3,1-cGNR, where the inset shows an STM scan on the ribbon and the crosses indicate the positions at which the spectra have been recorded. A spectrum recorded on the middle of the nanoribbon (green curve) shows resonances at −1.7, −1.3, 0.5, and 0.9 V. Additional peaks at −1.4, 0.7, 1.2, and 1.4 V are observed in spectra recorded on different points on the ribbon (orange, blue, and purple curves).

In order to establish the nature of the frontier states, differential conductance maps were recorded at the energetic positions of the peaks in the dI/dV spectroscopy and compared to simulated maps as obtained from tight-binding

calculations. From the theoretical perspective, it is clear that infinitely long 3,1-cGNRs have a relatively small band gap compared to that of 7-acGNRs, with low-energy bands that have a pronounced edge-localized character. This behavior is readily obtained in the edge-projected dispersion, local density of states, and crystal orbitals, as shown in Supplementary Figure S1. Similarly, calculations performed on the hexameric 3,1-cGNR return molecular orbitals around the Fermi energy that have a pronounced edge-localized character. Figure 2b shows simulated differential conductance maps of the states from HOMO−4 to LUMO+5 obtained from this model. Experimental differential conductance maps on the 6 monomer long 3,1-cGNR are shown in Figure 2c. Nine states could be accessed at different bias voltages, and the corresponding maps reveal the respective orbital shapes in detail. In particular, the edge-localized character is immediately apparent for all energy states. At positive bias voltage, the maps have distinct nodal plane structures along the length of the nanoribbons. States at negative bias feature some overlap due to their broadening, and therefore, some superposition is seen in the successive differential conductance maps that obscures the pattern for individual orbitals. Nevertheless, the simulated and experimental maps of the molecular orbitals are in good agreement.

We note that, in comparison with 3,1-cGNRs on Au(111), a more pronounced localization of the orbitals on the edges is observed.[57] This result is analogous to the decoupling of zigzag end-localized states in 7-acGNRs and edge-localized states in zigzag-type nanoribbons on NaCl.[21,47,50]

Conductance Mapping. Now, we turn to the charge transport properties of graphene nanoribbons. We will initially discuss the conductance experiments on 7-acGNRs. The GNR to be studied was lifted from the substrate by approaching the tip to the middle of one zigzag terminus of the GNR, contacting the nanoribbon (as evidenced by a jump in the current), and moving the tip vertically. During the lifting process, the opposite end is expected to remain nearly flat on the surface. These were synthesized from 10,10′-dibromo-9,9′-bianthryl, following the procedure of Cai *et al.*[17] Vertical and subsequent horizontal transfer onto NaCl was performed, and by acquiring $I(V)$ spectra for a range of tip heights, we

obtained dI/dV(V,z) maps of the conductance of 7-acGNR on NaCl on Au(111). This technique was applied to the 7-acGNR shown in Figure 3a,b (where it is imaged on sodium chloride).
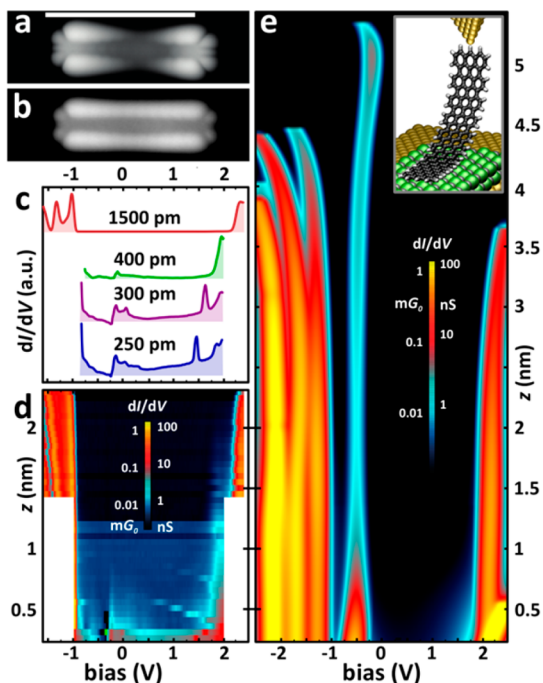

Figure 3. Conductance mapping of 7-acGNR on NaCl. (a) STM scan (V = −1.0 V, I = 20 pA) of a 5 monomer long 7-acGNR on NaCl on Au(111). Scale bar: 5 nm. (b) STM scan of the same ribbon as panel a, at V = −1.8 V, I = 20 pA. (c) dI/dV(V) spectra (cross sections of the map in panel d) on the 5 monomer long 7-acGNR for different values of the tip height z. (d) Conductance map dI/dV(V,z). (e) Simulated conductance map dI/dV(V,z) for the 5 monomer long 7-acGNR on NaCl on Au(111). The inset shows a model of the ribbon being lifted off the NaCl by the tip.

A few individual dI/dV(V) spectra at different heights are shown in Figure 3c. Figure 3d shows a two-dimensional contour plot of the conductance as a function of bias voltage and tip−sample distance (horizontal and vertical axis, respectively). A model of the nanoribbon being lifted off the

NaCl by the tip is shown in the inset of Figure 3e. It is clearly seen that the energy gap, where the conductance is essentially zero, is flanked by sharp onsets of resonant transport. Here, the conductance reaches values of over 100 nS, corresponding to approximately 2 per mille of the conductance quantum. This value is significantly lower than unimpeded molecular conductance as a result of the tunneling resistance of the NaCl. When the tip is retracted by more than 1.5 nm, peaks in the current transport are observed at approximately −1.0, −1.3, and 2.3 V. For very low tip heights, off-resonant transport is visible inside the gap, becoming negligible for a tip height of approximately 1.5 nm. For increasing tip heights, the energy gap becomes larger, with the transport resonances shifting away from the Fermi level. We find that the maximum currents these junctions can sustain are on the order of 100 nA; larger currents typically result in destruction of the junction. This limits the experimentally accessible bias voltage window. The main features of the maps are well reproduced in conductance experiments on various 7-acGNRs, as shown in Supplementary Figure S2. Discontinuities are occasionally observed in successive spectra, which may originate from lateral relaxations of the segment of the nanoribbon in contact with the surface with increasing tip height—a stick−slip effect. Nevertheless, the peak positions and conductance values remain relatively well-behaved. In addition to the differential conductance, determination of the current and its gradient in (V,z) space allows numerous transport quantities to be obtained. Supplementary Figure S3 shows the map of the current I(V,z) and the resistance R(V,z), as well as traces of the current, current decay dI/dz, conductance G = I/V, differential conductance, resistance R = V/I, and differential resistance dV/dI for the 7-acGNR of Figure 3. Notably, the resistance takes on values in the TΩ range in the band gap but drops to the MΩ range upon reaching the resonant regime.

The energy values corresponding to the onset of resonant transport are in quantitative agreement with the values found in spectroscopy experiments.[47] We therefore assume that the transport is mediated by the corresponding frontier orbitals. At the same time, this suggests that attaching the tip to the ribbon does not strongly affect the frontier states of the nanoribbon. This is in agreement with earlier work showing that the electronic structure of the ribbons is not significantly affected
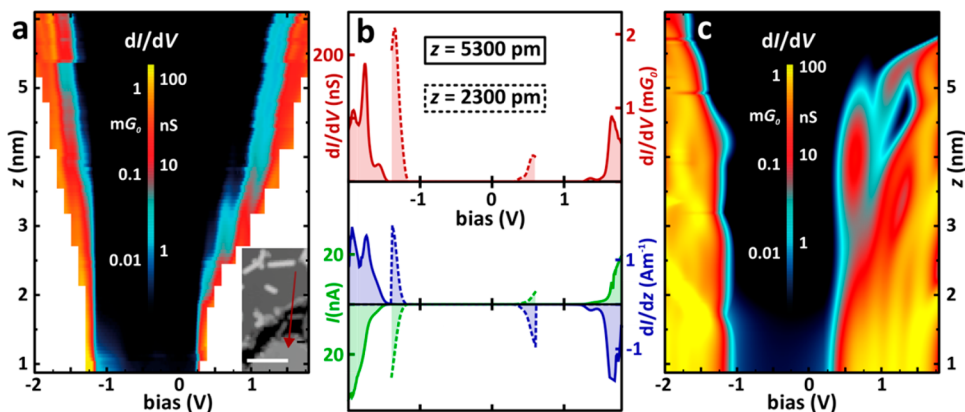

Figure 4. Conductance mapping of 3,1-cGNR on NaCl. (a) Conductance map dI/dV(V,z). The inset shows an STM scan (V = −1.8 V, I = 20 pA) of the 3,1-cGNR before manipulation onto the NaCl (manipulation indicated with the red arrow). Scale bar: 10 nm. (b) dI/dV(V) spectra (red), I(V) spectra (green), and dI/dz curves (blue) of the 3,1-cGNR at two different tip heights. The dashed curves (smaller bias window) correspond to the ribbon lifted to a height of 2300 pm, whereas the solid curves correspond to a tip height of 5300 pm. (c) Simulated conductance map dI/dV(V,z) for the 3,1-cGNR on NaCl on Cu(111).

by contacting a metallic lead.[58] The widening of the energy gap with increasing tip height can be understood in terms of capacitive effects. When the tip is lifted from the surface, the nanoribbon loses contact with the substrate, lowering the coupling of the nanoribbon to the substrate. This causes the relative coupling of the nanoribbon to the tip in comparison with the coupling to the surface to become more pronounced. By considering the double-junction system composed of a tip, substrate, and nanoribbon as a capacitive voltage divider,[59−61] it is evident that the voltage of the nanoribbon becomes more capacitively coupled to the voltage of the tip. Now a larger bias voltage needs to be applied to reach resonance, explaining the opening of the energy gap with increasing tip height.

To corroborate this picture, we performed transport simulations on GNRs within the framework of the non-equilibrium Green's function (NEGF) technique and the tight-binding model. In this model, the vacuum orbital energies are capacitively shifted from the vacuum energies by an amount given by the ratio of coupling to tip and surface (details are given in the Supporting Information). Figure 3e shows a simulated conductance map on the nanoribbon of Figure 3a–d. There is a strong resemblance between the simulated and the experimental map. In particular, the opening of the energy gap with increasing tip height is well reproduced. We note that the "phantom" transport channel near zero bias that arises in the simulation but not in the experiment is related to the end states of the nanoribbon, which are degenerate in the tight-binding model due to absence of explicit electron−electron interactions. In reality, these states are affected by coupling to the tip, lifting the degeneracy. In addition, they may be localized on either end and therefore do not contribute to transport.[43,62]

Having established the conductance characteristics of 7-acGNRs, we turned to the 3,1-cGNRs to apply the same methodology. In the same fashion as described above for 7-acGNRs, various 3,1-cGNRs were transferred onto NaCl, and conductance measurements were performed by recording $I(V)$ and $dI/dV(V)$ spectra for a range of tip heights z, again resulting in two-dimensional maps of the conductance in (V,z) space. Figure 4a shows a conductance map of a 3,1-cGNR. Cross sections of the map ($dI/dV(V)$, $dI/dz(V)$, and $I(V)$ spectra corresponding to two different tip heights) are shown in Figure 4b. A resistance map $R(V,z)$, dI/dV spectra corresponding to more tip heights, and a current map $I(V,z)$ are given in Supplementary Figure S4.

For the 3,1-cGNR, the onsets of resonant transport occur at −1.3 and 0.3 V. Similar to the case of 7-acGNRs, these values are in agreement with the energetic position of the HOMO and LUMO as obtained from spectroscopy measurements (see Figure 2a). We can therefore again draw the conclusion that the perturbing effect of the tip on the frontier states is relatively small and assume that the current transport at the resonant onsets is mediated by these orbitals. This shows that conductance maps of different nanoribbons immediately return transport characteristics that can be directly related to the electronic structure of the corresponding structures. The conductance maps consistently show onsets of conductance at the same bias voltages, the same magnitude of the (differential) conductance, and the same qualitative features and opening of the energy gap, regardless of tip apex shape or ribbon length (see Supplementary Figure S4).

For increasing tip heights, the energy gap widens, similar to the effect of 7-acGNRs on NaCl on Au(111). This effect is also observed in the simulation, as shown in Figure 4c. Although there is a qualitative agreement between the experimental and simulated conductance maps, the shifting of the transport resonances away from the Fermi energy is more uniform in the experiment than in the calculations. Moreover, we find that the energy gap widening with increasing tip height is almost independent of ribbon length. This hints toward a similar magnitude of capacitive coupling of conductance orbitals to the surface in short and long nanoribbons. We tentatively propose that the orbitals that play a role in transport are more strongly localized on the part of the nanoribbon between the tip and surface due to their bent geometry[43] and possibly an internal bias drop,[63] limiting the proportion of the orbitals in capacitive connection to the surface to a relatively short segment close to the point where the nanoribbon curves up from the surface. The simple tight-binding-based transport model used here does not take these effects into account. We expect more accurate models to yield a more quantitative resemblance. The above results show that the conductance profiles of different ribbons can be understood and simulated in terms of the different electronic structures of the respective ribbons and capacitive effects due to coupling to tip and substrate.

For both 7-acGNRs and 3,1-cGNRs, we also measured conductance maps on the bare metal surface. Three maps of 3,1-cGNRs on Cu(111) are shown in Supplementary Figure S6. Although the onsets of resonant transport could be observed, it was found that the large currents involved prevented us from increasing the bias voltage sufficiently far to be able to properly observe peaks related to resonant transport. Attempts to do so were repeatedly met with destruction of the junction. Furthermore—and especially in the case with 3,1-cGNRs—significant discontinuities are observed between successive spectra, likely originating from a severe stick−slip effect of the segment of the nanoribbon in contact with the surface, due to the strong interaction of the GNR with the metal. This underlines the necessity of intercalation in conductance experiments.

Double Modulation Spectroscopy. The final result relates to our further development of the conductance mapping methodology. In addition to the current I and the differential conductance dI/dV, another quantity of interest is the current decay with increasing tip height dI/dz. More specifically, an important parameter in the context of transport is the current decay parameter β, which is the proportionality constant in the exponential decay of current with tip height.

$$I(V, z) = I(V, z_0)e^{-\beta(z-z_0)}$$

For ballistic transport in the resonant regime, the current does not decay with junction length: β should vanish. However, the bent geometry of the ribbon in the junction can result in a nonzero value of the decay parameter, also during resonant transport.[43] Measurements of β have been instrumental in conductance measurements on GNRs.[33] Usually, β is extracted by fitting a $\ln(I)$ versus z plot. However, because β is a function of voltage, but may even depend on tip height (for example in the multiexponential decay in GNR heterojunctions[33]), a technique to measure $\beta(V,z)$ locally is desirable.

The differential conductance dI/dV can efficiently be obtained using a lock-in amplifying technique, where a modulation signal is added to the bias voltage. In the same spirit, in order to measure dI/dz, we subjected the z-

piezoelectric element of the tip to a modulation signal from a second lock-in amplifier. The resulting current through the junction can be described as

$$I(t) = I_0 + V_{mod}\frac{dI}{dV}e^{i\omega_V t} + z_{mod}\frac{dI}{dz}e^{i\omega_z t}$$

where I_0 is the discrete component of the tunnel current, V_{mod} and ω_V are the modulation amplitude and frequency of the voltage modulation, and z_{mod} and ω_z the amplitude and frequency of the tip-height modulation. After conversion of the tunnel current signal to a voltage by the control unit (CU), this signal can be distributed to the respective lock-in amplifiers, with each lock-in amplifier "selecting" the current component according to frequency. A schematic image of this setup is shown in Figure 5a. Finally, β is calculated as

$$\beta(V, z) = -\frac{\partial \ln I(V, z)}{\partial z} = -\left(\frac{1}{I(V, z)}\right)\frac{\partial I(V, z)}{\partial z}$$
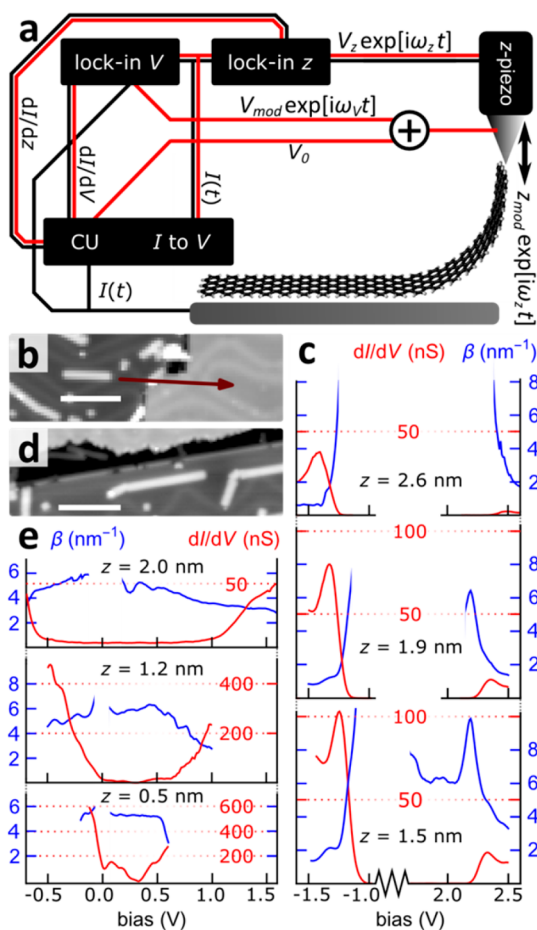

Figure 5. Conductance decay measurements using the double modulation technique. (a) Schematic setup of the lock-in amplifiers to modulate the bias voltage and tip height and record dI/dV and dI/dz simultaneously. (b) STM scan ($V = -1.8$ V, $I = 20$ pA) of a 7-acGNR which was subjected to double modulation spectroscopy experiments after transfer to NaCl (transfer indicated with the red arrow). (c) Conductance (red) and current decay (blue) for the ribbon of panel b on NaCl. (d) STM image of a 7-acGNR which was subjected to double modulation spectroscopy on Au(111). (e) Conductance (red) and current decay (blue) for the ribbon of panel d on Au(111).

The value of I is simply the discrete (or time-averaged) value of the tunnel current, and dI/dz is extracted from the tip-height modulating lock-in amplifier. The absence of cross-talk between the dI/dV and dI/dz signals was established by recording spectra on a 7-acGNR on NaCl on Au(111) with the separate lock-in signals switched on and off, as shown in Supplementary Figure S7.

This technique was used to simultaneously measure dI/dV and dI/dz on a 7-acGNR suspended between the tip and NaCl/Au(111) surface. Figure 5b shows an STM scan of a ribbon that was picked up and dragged onto a NaCl patch. Figure 5c shows spectra of the conductance (red) and the current decay parameter β (blue) at different tip–sample distances. As can clearly be seen, β is large inside the gap region (it diverges as the current becomes essentially zero) and decreases when resonant tunneling become accessible. At 2.63 nm, β is seen to decrease to values as low as 0.5 nm^{-1} (at voltages corresponding to tunneling through the HOMO), down from 2 nm^{-1} for the same transport channel at $z = 1.5$ nm. The faster decay of the transport channel on the positive bias side compared to the channel on the negative bias side manifests itself in a consistently higher value of β at the energies corresponding to the resonance found in the dI/dV. The fact that the conductance decay goes to zero for the HOMO resonance indicates that it obtains an increasingly ballistic character, and after an initial decrease in the conductance—possibly due to the curvature of the nanoribbon as the junction is in the formation stage[43]—further increase of the junction results does not suppress the current anymore. This suggests that the HOMO could contribute to long-range transport.[46]

As a further validation of this technique and in order to compare with established results, an experiment was carried out on the ribbon shown in Figure 5d, which was not dragged onto NaCl. Figure 5e shows dI/dV and dI/dz spectra, focusing on the low-bias regime at low tip heights. Similar to earlier studies, the value of β becomes 5 nm^{-1} for low bias or off-resonant transport. In addition to this off-resonant decay value, it can be seen that β diminishes when approaching onsets of resonance in the differential conductance, again in agreement with earlier experiments.[43] In contrast with earlier literature results, β can now be determined in a single continuous spectrum, rather than recording numerous $I(z)$ spectra and extracting a value through fitting. Moreover, β can be determined for precisely defined tip heights, even when the current decay with tip height is multiexponential due to the nanoribbons being segmented or transport resonances shifting in energy capacitively. We conclude that the double modulation spectroscopy technique allows for a voltage- and junction-length-dependent measurement of the current decay parameter, where the degree of ballistic transport can be found as a function of tip height and voltage in a single measurement.

CONCLUSIONS

We demonstrated successful electronic decoupling of different types of GNRs by STM-mediated transfer onto an intercalating layer of NaCl. STS measurements on electronically decoupled 3,1-cGNRs revealed the existence of edge-localized frontier states at low bias voltages. The spectroscopic analysis provided a benchmark for the electronic structure for comparison with conductance experiments. The conductance of individual GNRs was measured in lifting geometry, using the methodology developed by Koch et al.[43] Besides electronic decoupling,

the monolayer of NaCl acts as an additional tunnel barrier, minimizing the risk of current-induced defect formation and thereby facilitating the characterization of resonant transport along the long GNR axis. Too high currents can result in defective GNRs, presumably due to dehydrogenation of the edges and carbon—carbon bond cleavage, as well as ejection of tip material onto the surface/GNR. We mapped out the conductance of 7-acGNRs and 3,1-cGNRs in (V,z) space and observed transport through multiple resonant channels. The $dI/dV(V,z)$ maps provide detailed information on the conductance properties. The height dependence of the conductance can be explained in terms of the electronic structures of the specific types of GNRs and capacitive coupling to tip and substrate. Specifically, the widening of the energy gap with increasing tip height can be understood in terms of a decreasing coupling of molecular orbitals with the surface compared to the tip. This explanation was corroborated by transport calculations.

Finally, we demonstrated the feasibility of double modulation spectroscopy—simultaneously measuring the differential conductances dI/dV and dI/dz by making use of two separate lock-in amplifiers. The double modulation spectroscopy technique allowed for the simultaneous measurement of $I(V,z)$ and its gradient $\nabla I(V,z)$, from which the current decay β can readily be extracted. This parameter was shown to give a "degree" of resonance of transport, with $\beta = 5$ nm^{-1} returned as the well-known off-resonant transport value for 7-acGNRs on Au(111), and values decreasing to 0.5 nm^{-1} indicating that the transport channel obtains a more ballistic character.

METHODS

Conductance Mapping. After lifting the GNRs to the desired height z and laterally manipulating to the desired position, $I(V,z)$ current measurements were performed by recording $I(V)$ spectra for a series of tip heights z. Here, $z = 0$ corresponds to the lowest tip height that was used, where the tunnel current between the tip and metal surface, without a contacted nanoribbon, is 400 pA at a bias voltage of 10 mV. Each single $I(V)$ curve was followed by a tip height increment/decrement Δz of 20—100 pm. All measurements are performed at a resolution of $\Delta V = 10$ mV per point, regardless of bias range, and with an integration time of 50 ms per point. $dI/dV(V)$ spectra were obtained using a 819 Hz oscillating signal of amplitude 5 mV rms and 50 ms integration time per point. Numerical values of the differential conductance were obtained by scaling the dI/dV data to give the least-squares fit to the differential conductance obtained through numerically differentiating the $I(V)$ spectra. It was found that during the course of measurements, there is always a chance of drop down (detachment from the tip), pick up (irreversible attachment to the tip), tip crash, or current-induced destruction of single nanoribbons. In order to prevent the latter, the bias voltage range was dynamically adjusted during the course of measurements (where, in our experience, currents larger than approximately 100 nA give rise to an increased risk of detachments or defect formation due to inelastic processes). Following an experiment that takes around 2 or 3 h, going back to the feedback set-point revealed that the total drift is on the order of 100 pm. This is small in comparison with the range of the conductance maps.

Double Modulation Spectroscopy. The tip height was modulated with a 20 pm (peak-to-peak) oscillation amplitude at a frequency of 121 Hz, by application of the appropriate modulation voltage to the z-piezo of the STM.

Tight-Binding Calculations. The simulated differential conductance maps were obtained by diagonalizing a tight-binding Hamiltonian containing on-site energies ε_0 and nearest-neighbor hopping parameters t. We employed a 12% increase of the hopping

integral t for carbon atoms on the edge, so that $t_{ij}(\text{edge}) = 1.12\, t$ whenever atom i or j is bonded to at least one hydrogen atom. The simulated maps correspond to pure eigenstates, the orbitals of which are convolved with a Gaussian-shaped tip of width 1.2 Å to simulate the finite size of the STM tip. More information is given in the Supporting Information.

Conductance Map Simulations. For the simulated conductance maps, the nonequilibrium Green's function technique was applied in the wide-band limit,[33,64] in conjunction with the aforementioned tight-binding model. Here, we use a nearest-neighbor interaction parameter $t = -2.7$ eV[65] and an on-site energy of $\varepsilon_0 = 0.8$ eV for 7-acGNRs on Au(111) and $\varepsilon_0 = 0.2$ eV for 3,1-cGNRs on Cu(111), reflecting the Fermi energy difference of graphene *in vacuo* with respect to that of gold and copper.[66-70] We employ an empirical charging energy (difference between hole tunneling and electron tunneling) of 1.8 eV for 7-acGNRs and 1.4 eV for 3,1-cGNRs based on the size of the HOMO—LUMO gaps observed in spectroscopy[47,59] in comparison to the vacuum energies found from tight binding. The self-energies due to the substrate are $\sigma_{\text{sub}} = \Lambda + 1i$ meV, and those due to the tip are $\sigma_{\text{tip}} = \Lambda + 3i$ meV. The self-energies due to the substrate are spatially modulated to zero to simulate lifting. The real parts of the self-energies are $\Lambda = -0.6$ eV for 7-acGNRs on Au(111) and $\Lambda = -0.4$ eV for 3,1-cGNRs on Cu(111). The parametrization is schematically shown in Supplementary Figure S5. Broadening— primarily due to interaction with phonons in the NaCl—is taken into account by convolving the conductance map with a Gaussian peak with a width of 100 meV, similar to the peak widths observed in spectroscopy.[49] More information is given in the Supporting Information.

ASSOCIATED CONTENT

Ⓢ Supporting Information

The Supporting Information is available free of charge on the ACS Publications website at DOI: 10.1021/acsnano.8b02770.

    Additional experimental details, equations, and figures

    (PDF)

AUTHOR INFORMATION

Corresponding Author
*E-mail: i.swart@uu.nl.

ORCID Ⓘ
Peter H. Jacobse: 0000-0002-0777-6050

Author Contributions
P.H.J. and I.S. conceived the experiments which were performed by P.H.J. and M.J.J.M. The experimental data were evaluated by P.H.J., M.J.J.M., and I.S. Automation of the nanoribbon lifting procedure and conductance measurements were obtained by S.J.M.Z. Tight-binding and transport calculations were performed by P.H.J. All authors contributed to writing the manuscript.

Notes
The authors declare no competing financial interest.

ACKNOWLEDGMENTS

REFERENCES

(1) Novoselov, K. S.; Geim, A. K.; Morozov, S. V.; Jiang, D.; Zhang, Y.; Dubonos, S. V.; Grigorieva, I. V.; Firsov, A. A. Electric Field in Atomically Thin Carbon Films. *Science* **2004**, *306*, 666−669.

(2) Geim, A. K.; Novoselov, K. S. The Rise of Graphene. *Nat. Mater.* **2007**, *6*, 183−191.

(3) Castro Neto, A. H.; Guinea, F.; Peres, N. M. R.; Novoselov, K. S.; Geim, A. K. The Electronic Properties of Graphene. *Rev. Mod. Phys.* **2009**, *81*, 109−162.

(4) Nakada, K.; Fujita, M.; Dresselhaus, G.; Dresselhaus, M. S. Edge State in Graphene Ribbons: Nanometer Size Effect and Edge Shape Dependence. *Phys. Rev. B: Condens. Matter Mater. Phys.* **1996**, *54*, 17954−17961.

(5) Son, Y. W.; Cohen, M. L.; Louie, S. G. Energy Gaps in Graphene Nanoribbons. *Phys. Rev. Lett.* **2006**, *97*, 216803.

(6) Yang, L.; Park, C. H.; Son, Y. W.; Cohen, M. L.; Louie, S. G. Quasiparticle Energies and Band Gaps in Graphene Nanoribbons. *Phys. Rev. Lett.* **2007**, *99*, 186801.

(7) Wakabayashi, K.; Sasaki, K.; Nakanishi, T.; Enoki, T. Electronic States of Graphene Nanoribbons and Analytical Solutions. *Sci. Technol. Adv. Mater.* **2010**, *11*, 054504.

(8) Narita, A.; Feng, X.; Müllen, K. Bottom-up Synthesis of Chemically Precise Graphene Nanoribbons. *Chem. Rec.* **2015**, *15*, 295−309.

(9) Narita, A.; Wang, X.-Y.; Feng, X.; Müllen, K. New Advances in Nanographene Chemistry. *Chem. Soc. Rev.* **2015**, *44*, 6616−6643.

(10) Lindner, R.; Kühnle, A. On-Surface Reactions. *ChemPhysChem* **2015**, *16*, 1582−1592.

(11) Shen, Q.; Gao, H.-Y.; Fuchs, H. Frontiers of On-Surface Synthesis: From Principles to Applications. *Nano Today* **2017**, *13*, 77−96.

(12) Nguyen, G. D.; Toma, F. M.; Cao, T.; Pedramrazi, Z.; Chen, C.; Rizzo, D. J.; Joshi, T.; Bronner, C.; Chen, Y. C.; Favaro, M.; Louie, S. G.; Fischer, F. R.; Crommie, M. F. Bottom-Up Synthesis of N = 13 Sulfur-Doped Graphene Nanoribbons. *J. Phys. Chem. C* **2016**, *120*, 2684−2687.

(13) Cloke, R. R.; Marangoni, T.; Nguyen, G. D.; Joshi, T.; Rizzo, D. J.; Bronner, C.; Cao, T.; Louie, S. G.; Crommie, M. F.; Fischer, F. R. Site-Specific Substitutional Boron Doping of Semiconducting Armchair Graphene Nanoribbons. *J. Am. Chem. Soc.* **2015**, *137*, 8872−8875.

(14) Kawai, S.; Saito, S.; Osumi, S.; Yamaguchi, S.; Foster, A. S.; Spijker, P.; Meyer, E. Atomically Controlled Substitutional Boron-Doping of Graphene Nanoribbons. *Nat. Commun.* **2015**, *6*, 8098.

(15) Talirz, L.; Söde, H.; Dumslaff, T.; Wang, S.; Sanchez-Valencia, J. R.; Liu, J.; Shinde, P.; Pignedoli, C. A.; Liang, L.; Meunier, V.; Plumb, N. C.; Shi, M.; Feng, X.; Narita, A.; Müllen, K.; Fasel, R.; Ruffieux, P. On-Surface Synthesis and Characterization of 9-Atom Wide Armchair Graphene Nanoribbons. *ACS Nano* **2017**, *11*, 1380−1388.

(16) Kimouche, A.; Ervasti, M. M.; Drost, R.; Halonen, S.; Harju, A.; Joensuu, P. M.; Sainio, J.; Liljeroth, P. Ultra-Narrow Metallic Armchair Graphene Nanoribbons. *Nat. Commun.* **2015**, *6*, 10177.

(17) Cai, J.; Ruffieux, P.; Jaafar, R.; Bieri, M.; Braun, T.; Blankenburg, S.; Muoth, M.; Seitsonen, A. P.; Saleh, M.; Feng, X.; Müllen, K.; Fasel, R. Atomically Precise Bottom-up Fabrication of Graphene Nanoribbons. *Nature* **2010**, *466*, 470−473.

(18) Zhang, H.; Lin, H.; Sun, K.; Chen, L.; Zagranyarski, Y.; Aghdassi, N.; Duhm, S.; Li, Q.; Zhong, D.; Li, Y.; Müllen, K.; Fuchs, H.; Chi, L. On-Surface Synthesis of Rylene-Type Graphene Nanoribbons. *J. Am. Chem. Soc.* **2015**, *137*, 4022−4025.

(19) Basagni, A.; Sedona, F.; Pignedoli, C. A.; Cattelan, M.; Nicolas, L.; Casarin, M.; Sambi, M. Molecules-Oligomers-Nanowires-Graphene Nanoribbons: A Bottom-up Stepwise on-Surface Covalent Synthesis Preserving Long-Range Order. *J. Am. Chem. Soc.* **2015**, *137*, 1802−1808.

(20) Chen, Y. C.; De Oteyza, D. G.; Pedramrazi, Z.; Chen, C.; Fischer, F. R.; Crommie, M. F. Tuning the Band Gap of Graphene Nanoribbons Synthesized from Molecular Precursors. *ACS Nano* **2013**, *7*, 6123−6128.

(21) Ruffieux, P.; Wang, S.; Yang, B.; Sanchez-Sanchez, C.; Liu, J.; Dienel, T.; Talirz, L.; Shinde, P.; Pignedoli, C. A.; Passerone, D.; Dumslaff, T.; Feng, X.; Müllen, K.; Fasel, R. On-Surface Synthesis of Graphene Nanoribbons with Zigzag Edge Topology. *Nature* **2016**, *531*, 489−492.

(22) Liu, J.; Li, B.-W.; Tan, Y.-Z.; Giannakopoulos, A.; Sanchez-Sanchez, C.; Beljonne, D.; Ruffieux, P.; Fasel, R.; Feng, X.; Müllen, K. Toward Cove-Edged Low Band Gap Graphene Nanoribbons. *J. Am. Chem. Soc.* **2015**, *137*, 6097−6103.

(23) Han, P.; Akagi, K.; Federici Canova, F.; Mutoh, H.; Shiraki, S.; Iwaya, K.; Weiss, P. S.; Asao, N.; Hitosugi, T. Bottom-up Graphene-Nanoribbon Fabrication Reveals Chiral Edges and Enantioselectivity. *ACS Nano* **2014**, *8*, 9181−9187.

(24) Han, P.; Akagi, K.; Federici Canova, F.; Shimizu, R.; Oguchi, H.; Shiraki, S.; Weiss, P. S.; Asao, N.; Hitosugi, T. Self-Assembly Strategy for Fabricating Connected Graphene Nanoribbons. *ACS Nano* **2015**, *9*, 12035−12044.

(25) Sánchez-Sánchez, C.; Dienel, T.; Deniz, O.; Ruffieux, P.; Berger, R.; Feng, X.; Müllen, K.; Fasel, R. Purely Armchair or Partially Chiral: Noncontact Atomic Force Microscopy Characterization of Dibromo-Bianthryl-Based Graphene Nanoribbons Grown on Cu(111). *ACS Nano* **2016**, *10*, 8006−8011.

(26) Schulz, F.; Jacobse, P. H.; Canova, F. F.; van der Lit, J.; Gao, D. Z.; van den Hoogenband, A.; Han, P.; Klein Gebbink, R. J. M.; Moret, M. E.; Joensuu, P. M.; Swart, I.; Liljeroth, P. Precursor Geometry Determines the Growth Mechanism in Graphene Nanoribbons. *J. Phys. Chem. C* **2017**, *121*, 2896−2904.

(27) De Oteyza, D. G.; García-Lekue, A.; Vilas-Varela, M.; Merino-Díez, N.; Carbonell-Sanromà, E.; Corso, M.; Vasseur, G.; Rogero, C.; Guitián, E.; Pascual, J. I.; Ortega, J. E.; Wakayama, Y.; Peña, D. Substrate-Independent Growth of Atomically Precise Chiral Graphene Nanoribbons. *ACS Nano* **2016**, *10*, 9000−9008.

(28) Fujita, M.; Wakabayashi, K.; Nakada, K.; Kusakabe, K. Peculiar Localized State at Zigzag Graphite Edge. *J. Phys. Soc. Jpn.* **1996**, *65*, 1920−1923.

(29) Tao, C.; Jiao, L.; Yazyev, O. V.; Chen, Y. C.; Feng, J.; Zhang, X.; Capaz, R. B.; Tour, J. M.; Zettl, A.; Louie, S. G.; Dai, H.; Crommie, M. F. Spatially Resolving Edge States of Chiral Graphene Nanoribbons. *Nat. Phys.* **2011**, *7*, 616−620.

(30) Jiang, Z.; Song, Y. Band Gap Oscillation and Novel Transport Property in Ultrathin Chiral Graphene Nanoribbons. *Phys. B* **2015**, *464*, 61−67.

(31) Carvalho, A. R.; Warnes, J. H.; Lewenkopf, C. H. Edge Magnetization and Local Density of States in Chiral Graphene Nanoribbons. *Phys. Rev. B: Condens. Matter Mater. Phys.* **2014**, *89*, 245444.

(32) Sun, L.; Wei, P.; Wei, J.; Sanvito, S.; Hou, S. From Zigzag to Armchair: The Energetic Stability, Electronic and Magnetic Properties of Chiral Graphene Nanoribbons with Hydrogen-Terminated Edges. *J. Phys.: Condens. Matter* **2011**, *23*, 425301.

(33) Jacobse, P. H.; Kimouche, A.; Gebraad, T.; Ervasti, M. M.; Thijssen, J. M.; Liljeroth, P.; Swart, I. Electronic Components Embedded in a Single Graphene Nanoribbon. *Nat. Commun.* **2017**, *8*, 119.

(34) Blankenburg, S.; Cai, J.; Ruffieux, P.; Jaafar, R.; Passerone, D.; Feng, X.; Müllen, K.; Fasel, R.; Pignedoli, C. A. Intraribbon Heterojunction Formation in Ultranarrow Graphene Nanoribbons. *ACS Nano* **2012**, *6*, 2020−2025.

(35) Chen, Y. C.; Cao, T.; Chen, C.; Pedramrazi, Z.; Haberer, D.; De Oteyza, D. G.; Fischer, F. R.; Louie, S. G.; Crommie, M. F. Molecular Bandgap Engineering of Bottom-up Synthesized Graphene Nanoribbon Heterojunctions. *Nat. Nanotechnol.* **2015**, *10*, 156−160.

(36) Wang, S.; Kharche, N.; Costa Girão, E.; Feng, X.; Müllen, K.; Meunier, V.; Fasel, R.; Ruffieux, P. Quantum Dots in Graphene Nanoribbons. *Nano Lett.* **2017**, *17*, 4277−4283.

(37) Bronner, C.; Durr, R. A.; Rizzo, D. J.; Lee, Y.-L.; Marangoni, T.; Kalayjian, A. M.; Rodriguez, H.; Zhao, W.; Louie, S. G.; Fischer, F. R.;

Crommie, F. R. Hierarchical On-Surface Synthesis of Graphene Nanoribbon Heterojunctions. *ACS Nano* **2018**, *12*, 2193−2200.

(38) Cai, J.; Pignedoli, C. A.; Talirz, L.; Ruffieux, P.; Söde, H.; Liang, L.; Meunier, V.; Berger, R.; Li, R.; Feng, X.; Müllen, K.; Fasel, R. Graphene Nanoribbon Heterojunctions. *Nat. Nanotechnol.* **2014**, *9*, 896−900.

(39) Nguyen, G. D.; Tsai, H. Z.; Omrani, A. A.; Marangoni, T.; Wu, M.; Rizzo, D. J.; Rodgers, G. F.; Cloke, R. R.; Durr, R. A.; Sakai, Y.; Liou, F.; Aikawa, A. S.; Chelikowsky, J. R.; Louie, S. G.; Fischer, F. R.; Crommie, M. F. Atomically Precise Graphene Nanoribbon Heterojunctions from a Single Molecular Precursor. *Nat. Nanotechnol.* **2017**, *12*, 1077−1082.

(40) Huang, B.; Yan, Q. M.; Li, Z. Y.; Duan, W. H. Towards Graphene Nanoribbon-Based Electronics. *Front. Phys. China* **2009**, *4*, 269−279.

(41) Bennett, P. B.; Pedramrazi, Z.; Madani, A.; Chen, Y. C.; De Oteyza, D. G.; Chen, C.; Fischer, F. R.; Crommie, M. F.; Bokor, J. Bottom-up Graphene Nanoribbon Field-Effect Transistors. *Appl. Phys. Lett.* **2013**, *103*, 253114.

(42) Llinas, J. P.; Fairbrother, A.; Borin Barin, G.; Shi, W.; Lee, K.; Wu, S.; Yong Choi, B.; Braganza, R.; Lear, J.; Kau, N.; Choi, W.; Chen, C.; Pedramrazi, Z.; Dumslaff, T.; Narita, A.; Feng, X.; Müllen, K.; Fischer, F. R.; Zettl, A.; Ruffieux, P.; et al. Short-Channel Field-Effect Transistors with 9-Atom and 13-Atom Wide Graphene Nanoribbons. *Nat. Commun.* **2017**, *8*, 633.

(43) Koch, M.; Ample, F.; Joachim, C.; Grill, L. Voltage-Dependent Conductance of a Single Graphene Nanoribbon. *Nat. Nanotechnol.* **2012**, *7*, 713−717.

(44) Lafferentz, L.; Ample, F.; Yu, H. B.; Hecht, S.; Joachim, C.; Grill, L. Conductance of a Single Conjugated Polymer as a Continuous Function of Its Length. *Science* **2009**, *323*, 1193−1197.

(45) Nacci, C.; Ample, F.; Bleger, D.; Hecht, S.; Joachim, C.; Grill, L. Conductance of a Single Flexible Molecular Wire Composed of Alternating Donor and Acceptor Units. *Nat. Commun.* **2015**, *6*, 7397.

(46) Kuang, G.; Chen, S. Z.; Wang, W.; Lin, T.; Chen, K.; Shang, X.; Liu, P. N.; Lin, N. Resonant Charge Transport in Conjugated Molecular Wires beyond 10 Nm Range. *J. Am. Chem. Soc.* **2016**, *138*, 11140−11143.

(47) Wang, S.; Talirz, L.; Pignedoli, C. A.; Feng, X.; Müllen, K.; Fasel, R.; Ruffieux, P. Giant Edge State Splitting at Atomically Precise Graphene Zigzag Edges. *Nat. Commun.* **2016**, *7*, 11507.

(48) Deniz, O.; Sánchez-Sánchez, C.; Dumslaff, T.; Feng, X.; Narita, A.; Müllen, K.; Kharche, N.; Meunier, V.; Fasel, R.; Ruffieux, P. Revealing the Electronic Structure of Silicon Intercalated Armchair Graphene Nanoribbons by Scanning Tunneling Spectroscopy. *Nano Lett.* **2017**, *17*, 2197−2203.

(49) Repp, J.; Meyer, G.; Stojković, S. M.; Gourdon, A.; Joachim, C. Molecules on Insulating Films: Scanning-Tunneling Microscopy Imaging of Individual Molecular Orbitals. *Phys. Rev. Lett.* **2005**, *94*, 026803.

(50) Bombis, C.; Ample, F.; Lafferentz, L.; Yu, H.; Hecht, S.; Joachim, C.; Grill, L. Single Molecular Wires Connecting Metallic and Insulating Surface Areas. *Angew. Chem., Int. Ed.* **2009**, *48*, 9966−9970.

(51) Kawai, S.; Benassi, A.; Gnecco, E.; Söde, H.; Pawlak, R.; Feng, X.; Müllen, K.; Passerone, D.; Pignedoli, C. A.; Ruffieux, P.; Fasel, R.; Meyer, E. Superlubricity of Graphene Nanoribbons on Gold Surfaces. *Science* **2016**, *351*, 957−961.

(52) Björk, J.; Stafström, S.; Hanke, F. Zipping up: Cooperativity Drives the Synthesis of Graphene Nanoribbons. *J. Am. Chem. Soc.* **2011**, *133*, 14884−14887.

(53) Ruffieux, P.; Cai, J.; Plumb, N. C.; Patthey, L.; Prezzi, D.; Ferretti, A.; Molinari, E.; Feng, X.; Müllen, K.; Pignedoli, C. A.; Fasel, R. Electronic Structure of Atomically Precise Graphene Nanoribbons. *ACS Nano* **2012**, *6*, 6930−6935.

(54) Söde, H.; Talirz, L.; Gröning, O.; Pignedoli, C. A.; Berger, R.; Feng, X.; Müllen, K.; Fasel, R.; Ruffieux, P. Electronic Band Dispersion of Graphene Nanoribbons *via* Fourier-Transformed Scanning Tunneling Spectroscopy. *Phys. Rev. B: Condens. Matter Mater. Phys.* **2015**, *91*, 045429.

(55) Akhmerov, A. R.; Beenakker, C. W. J. Boundary Conditions for Dirac Fermions on a Terminated Honeycomb Lattice. *Phys. Rev. B: Condens. Matter Mater. Phys.* **2008**, *77*, 085423.

(56) Wimmer, M.; Akhmerov, A. R.; Guinea, F. Robustness of Edge States in Graphene Quantum Dots. *Phys. Rev. B: Condens. Matter Mater. Phys.* **2010**, *82*, 045409.

(57) Merino-Díez, N.; Li, J.; Garcia-Lekue, A.; Vasseur, G.; Vilas-Varela, M.; Carbonell-Sanromà, E.; Corso, M.; Ortega, J. E.; Peña, D.; Pascual, J. I.; De Oteyza, D. G. Unraveling the Electronic Structure of Narrow Atomically Precise Chiral Graphene Nanoribbons. *J. Phys. Chem. Lett.* **2018**, *9*, 25−30.

(58) van der Lit, J.; Boneschanscher, M. P.; Vanmaekelbergh, D.; Ijäs, M.; Uppstu, A.; Ervasti, M.; Harju, A.; Liljeroth, P.; Swart, I. Suppression of Electron-Vibron Coupling in Graphene Nanoribbons Contacted *via* a Single Atom. *Nat. Commun.* **2013**, *4*, 2023.

(59) Swart, I.; Gross, L.; Liljeroth, P. Single-Molecule Chemistry and Physics Explored by Low-Temperature Scanning Probe Microscopy. *Chem. Commun.* **2011**, *47*, 9011.

(60) Nazin, G. V.; Wu, S. W.; Ho, W. Tunneling Rates in Electron Transport through Double-Barrier Molecular Junctions in a Scanning Tunneling Microscope. *Proc. Natl. Acad. Sci. U. S. A.* **2005**, *102*, 8832−8837.

(61) Nitzan, A.; Ratner, M. A. Electron Transport in Molecular Wire Junctions. *Science* **2003**, *300*, 1384−1389.

(62) Ijäs, M.; Ervasti, M.; Uppstu, A.; Liljeroth, P.; van der Lit, J.; Swart, I.; Harju, A. Electronic States in Finite Graphene Nanoribbons: Effect of Charging and Defects. *Phys. Rev. B: Condens. Matter Mater. Phys.* **2013**, *88*, 075429.

(63) Liang, G. C.; Ghosh, A. W.; Paulsson, M.; Datta, S. Electrostatic Potential Profiles of Molecular Conductors. *Phys. Rev. B: Condens. Matter Mater. Phys.* **2004**, *69*, 115302.

(64) Haug, H.; Jauho, A.-P. *Quantum Kinetics in Transport and Optics of Semiconductors*; Springer: Berlin, 2008; Vol. 6.

(65) Kundu, R. Tight-Binding Parameters for Graphene. *Mod. Phys. Lett. B* **2011**, *25*, 163−173.

(66) Haas, G. A.; Thomas, R. E. Work Function and Secondary Emission Studies of Various Cu Crystal Faces. *J. Appl. Phys.* **1977**, *48*, 86−93.

(67) Pescia, D.; Meier, F. Spin Polarized Photoemission from Gold Using Circularly Polarized Light. *Surf. Sci.* **1982**, *117*, 302−309.

(68) Sławińska, J.; Wlasny, I.; Dabrowski, P.; Klusek, Z.; Zasada, I. Doping Domains in Graphene on Gold Substrates: First-Principles and Scanning Tunneling Spectroscopy Studies. *Phys. Rev. B: Condens. Matter Mater. Phys.* **2012**, *85*, 235430.

(69) Barone, V.; Peralta, J. E.; Uddin, J.; Scuseria, G. E. Screened Exchange Hybrid Density-Functional Theory Study of the Work Function of Pristine and Doped Single-Wall Nanotubes. *J. Chem. Phys.* **2006**, *124*, 024709.

(70) Ishii, H.; Oji, H.; Ito, E.; Hayashi, N.; Yoshimura, D.; Seki, K. Energy Level Alignment and Band Bending at Model Interfaces of Organic Electroluminescent Devices. *J. Lumin.* **2000**, *87*, 61−65.